On the role of Zr and B addition on solidification cracking of IN738LC produced by laser powder bed fusion

Materialia 26 (2022) 101609

Contents lists available at ScienceDirect

Materialia

journal homepage: www.elsevier.com/locate/mtla

Full Length Article

On the role of Zr and B addition on solidification cracking of IN738LC produced by laser powder bed fusion

Kristina Lindgren[a], Fiona Schulz[b,1,*], Hans Gruber[b], Andreas Markström[c], Eduard Hryha[b]

[a] Department of Physics, Chalmers University of Technology, Göteborg SE-412 96, Sweden
[b] Department of Industrial and Materials Science, Chalmers University of Technology, Göteborg SE-412 96, Sweden
[c] Thermo-Calc Software AB, Solna SE-169 67, Sweden

ARTICLE INFO

Keywords:
Laser powder bed fusion (LPBF)
IN738LC
Atom probe tomography (APT)
Solidification cracking

ABSTRACT

The demand for manufacturing increasingly complex geometries for high temperature applications drives the increasing interest into additive manufacturing of nickel-based superalloys. Of particular interest are superalloys with high contents of the strengthening phase γ' such as IN738LC. Previous research suggests that especially B and Zr have a detrimental influence on crack formation during the laser powder bed fusion (LPBF) process. The present study investigates solidification cracks in an IN738LC derivative with increased B (0.03 wt.%) and Zr (0.07 wt.%) in more detail using high resolution techniques such as transmission electron microscopy (TEM) and atom probe tomography (APT). Analysis of the bulk material shows a high number of MC carbides containing Ti and Cr. The concentration profiles indicate non-equilibrium carbide compositions by suggesting that Cr is pushed out of these particles. The carbides are surrounded by a thin B-rich layer at the metal/carbide interface. Analysis of the fracture surface shows both Zr and small amounts of B in the formed oxide layer. The presence of these elements together with thermodynamic calculations and previously reported findings of the same material variant support the hypothesis that low-melting phases are likely reasons for cracking of IN738LC.

1. Introduction

Higher operating temperatures mean higher efficiencies for gas turbines which require high performing nickel-based superalloys for components such as stationary guide vanes or rotating turbine blades. The potential of manufacturing increasingly complex geometries for these applications drives the investigation into additive manufacturing (AM) of nickel-based superalloys with γ' volume fractions of 40–80% such as IN738LC or CM247LC [1–3]. Several studies have shown that cracking occurs in such superalloys when manufactured by means of electron beam melting (EBM) and laser powder bed fusion (LPBF) [3–6], newly termed PBF-EB and PBF-LB, respectively, according to ASTM standard 52,900–2021.

In welding, this susceptibility to cracking is attributed to the Al+Ti content of the alloy composition and cracking mechanisms range from solidification and liquation cracking to strain age and ductility dip cracking [7,8]. However, literature suggests that the large cracking susceptibility of hard-to-weld alloys during AM cannot be sufficiently explained by the Al+Ti content alone and is more closely linked to secondary phases which form during solidification of the material [2–6]. Both initiation and propagation of cracking observed in non-weldable superalloys during AM are closely related to high angle grain boundaries (HAGBs) [9,10]. The local composition along these grain boundaries was found to lead to liquid films during the final stages of solidification [10]. Two elements, B and Zr, stood out in their potential contribution to the cracking susceptibility of these alloys along the grain boundaries [2,4,5,11,12]. Both B and Zr are added to nickel-based superalloys for enhanced creep and tensile properties and better fluidity during casting. Cast IN738LC material is sensitive to the Zr content which was found to promote hot tearing [13]. The addition of Zr also showed significant influence on hot-cracking when processing high γ' containing nickel-based superalloys with LPBF [5,14].

Within AM superalloys, B was found to segregate as boride films along HAGBs which led to increased cracking susceptibility when manufacturing non-weldable nickel-based superalloys [2,4,5]. Boron was also detected as $(Cr,Mo)_3B_2$ and $(Cr,Mo)_5B_3$ in the bulk material [15], as well as in the form of Mo- and Cr-rich, off-stochiometric boride precursors along HAGBs [4]. Zr, another critical micro-alloying element in this alloy, was previously found on grain boundaries of LPBF manufactured IN738LC [5], as well as in γ' precipitates formed on grain boundaries in as-built material [14], and segregated as intermetallic phase Ni_7Zr_2 [15]. In addition to these phases containing B and Zr, Ti-rich MC-type

* Corresponding author.
E-mail address: fiona.schulz@unibw.de (F. Schulz).
[1] Present address: Institute of Materials Science, Universität der Bundeswehr München, DE-85577 Neubiberg, Germany.

https://doi.org/10.1016/j.mtla.2022.101609
Received 1 August 2022; Accepted 21 October 2022
Available online 22 October 2022

Table 1
Powder composition, given in both wt.% and at.%.

	B	Zr	Cr	Co	Al	Ti	W	Ta	Mo	Nb	Fe	C	Ni
wt.%	0.03	0.07	16.0	9.3	3.2	3.3	2.9	1.73	1.72	0.9	<0.05	0.11	Bal.
at.%	0.16	0.04	17.55	9.0	6.76	3.93	0.9	0.55	1.02	0.55	<0.05	0.52	Bal.

carbides are known to form in as-built AM nickel-based superalloys. These carbides were found in the bulk and interdendritic regions, as well as in some cases in connection to small alumina (Al_2O_3) particles, or next to the borides mentioned above [15].

In a previous study, various derivatives of IN738LC were investigated with respect to their B and Zr content and their manufacturability during LPBF [16]. It was shown that both elements have a negative effect on the cracking susceptibility of the material, resulting in the highest crack density for the alloy with both high B (0.03 wt.%) and high Zr (0.07 wt.%) contents. The microcrack surfaces, located at HAGBs, displayed a dendritic structure which suggests that they are a consequence of solidification cracking [2]. Additionally, many secondary phase particles were observed on the fracture surfaces. The microcrack surfaces were analysed after fracturing the material specimens through bending in an ultra-high vacuum chamber, with the same methodology as described in [17]. X-ray photoelectron spectroscopy (XPS) analysis confirmed the presence of B and Zr containing oxides on the powder particles as well as on the fracture surfaces of this alloy. Auger electron spectroscopy (AES) analysis suggested that the presence of both B and Zr was limited to the microcrack surfaces with a higher oxygen content compared to reference areas on the fracture surface.

Due to the complex thermal history of nickel-based superalloys manufactured by LPBF [18], microstructural features such as the particles present on the microcrack surfaces are difficult to clearly determine. This follow-up study investigates the surface of the solidification cracks in more detail and aims to clarify the previous findings of the high B and Zr IN738LC derivative. While the above cited research investigated element segregation and precipitation to HAGBs, both this and the earlier study [16] focus on the analysis of the solidification crack surfaces. To allow for detailed analysis of the phases present on the microcrack surfaces, high resolution analysis techniques such as transmission electron microscopy (TEM) and atom probe tomography (APT) are used to identify the role of different elements and secondary phases within the material on the solidification cracking of as-built IN738LC.

2. Material and methods

2.1. Material

The material investigated was manufactured from spherical, gas atomized IN738LC powder with high B and high Zr contents (HB-HZr) (see Table 1). The powder with a size distribution of 25-63 μm was produced by Höganäs AB, Sweden, using a pilot vacuum induction gas atomizer (VIGA) with argon as atomizing gas.

As described in the previous study [16], the concentration of the trace elements S, P, Si, Mn, and O which are known to be detrimental to the cracking susceptibility of nickel base superalloys, was strictly controlled according to strict requirements within the AM industry (see Table 2).

2.2. Methods

Material cubes ($10 \times 10 \times 10$ mm^3) were produced by means of LPBF using an EOS M100 machine equipped with a 200 W laser and a laser spot size of 40 μm. The laser scan direction was rotated by 67° for each layer and the process parameters of 135 W laser power, 1150 mm/s scanning speed, 60 μm hatch distance, and a layer thickness of 20 μm were applied. All samples were produced with virgin powder in Argon atmosphere with $O_2 \leq 0.1\%$.

Table 2
Concentration of S, P, Si, Mn, and O in the powder measured by induction coupled plasma optical emission spectroscopy (ICP-OES), given in both wt.% and at.%.

	S	P	Si	Mn	O
wt.%	0.002	0.007	0.027	0.1	0.015
at.%	0.004	0.013	0.55	0.1	0.053

Samples were prepared metallographically to final polishing with OPA-solution for initial microscopic analysis using a field-emission LEO Gemini high resolution SEM equipped with a secondary electron in-lens detector.

APT and TEM specimens were prepared using a FEI Versa 3D Focused Ion Beam/Scanning Electron Microscope (FIB/SEM). The specimens were prepared from a fractured sample cross-section parallel to the build direction and close to the solidification crack surface, in the bulk of the printed part. TEM was performed in a FEI Titan 80–300 operated at 300 kV, with an Oxford X-sight X-ray detector. TIA software was used for EDX evaluation. High angle annular darkfield (HAADF) in scanning transmission electron microscopy (STEM) mode was used for imaging.

For the APT specimens, the sample surface was sputter coated with 70 nm of gold to enable analysis of the actual specimen surface. The printed part was fractured in air at room temperature and then coated. The APT specimens were prepared by a standard APT lift-out technique finished with annular milling and a 5 kV polish to remove Ga contamination and ion damage [19,20]. The locations of the lift-outs were chosen from the fracture surface to be in the previous solidification cracks, where the dendritic arms and previously observed particles [16] were present.

APT analysis was performed in an Imago LEAP 3000X HR, pulsed at 100–200 kHz. For most analyses, laser pulsing with energies of 0.3–0.5 nJ were used. For the metal matrix composition, voltage pulsed runs with 20% pulse fractions were used. The specimen temperature was kept between 30 and 60 K. The APT data were evaluated using IVAS 3.6.14. For the APT reconstruction, the image compression factor (ICF) was 1.65, the k-factor was 4.5, and the field was assumed to be 25 V/nm for laser pulsed runs, and 35 V/nm for voltage pulsed runs. Using these parameters, the reconstructions did not appear elongated or compressed. During the APT analysis, most of the Au from the 70 nm thick layer evaporated as Au^+, that correspond to an evaporation field below 27 V/nm according to Kingham curves [21,22]. The observed field of pure Au is 35 V/nm [23,24] when pulsed by voltage, making the assumption of a field lower than this during laser pulsing probable. Thus, the evaporation field of Au is most likely similar to the metal, estimated to be 25 V/nm. The use of Au as coating for APT specimen preparation of surfaces has the benefit of helping to aim for the surface during FIB milling due to the high contrast. However, the Au tend to evaporate in bursts, and the layer contains pores observed in FIB/SEM. In this paper, no significance is put to the distribution of Au in APT reconstructions.

Compositions of oxides, carbides, and borides were decided after cutting out the feature of interest from the main analysis using isoconcentration surfaces, and carefully deconvoluting the peaks of the mass

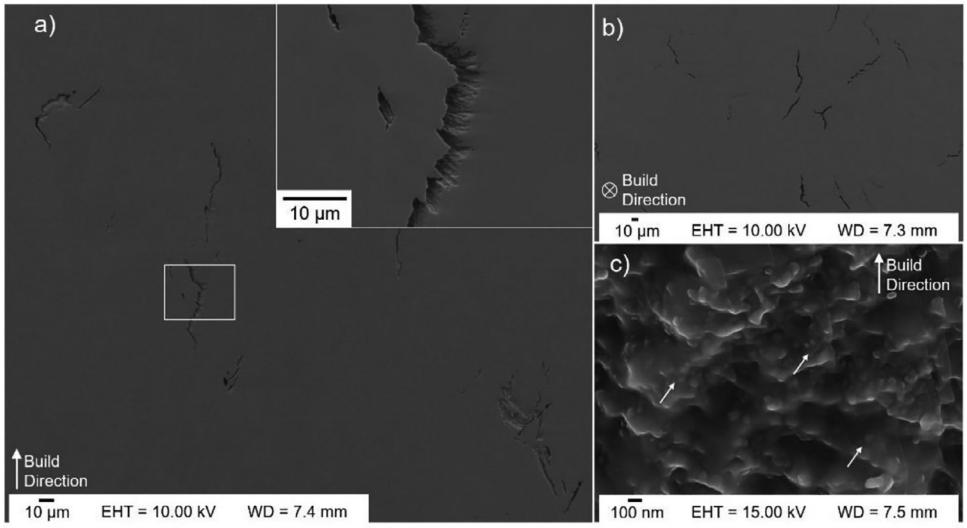

Fig. 1. SEM micrographs parallel (a) and perpendicular (b) to the build direction. High magnification of the solidification crack surface micrograph (c) shows dendritic arms and a high density of small particles (ca. 25-100 nm, indicated with small arrows) are visible on the surface.

spectra of the local volume. The errors given are either counting error or the variation between different analyses. Proximity histograms (proxigrams) [25] were used to show the concentration of different elements at different distances from specified isoconcentration surfaces.

APT analysis of the C content of carbides is usually slightly underrepresentative due to cascades of C evaporating and the deadtime of the detector [26]. This can be compensated for by using the natural abundance of C-13, which is less abundant than C-12 (1.1% and 98.9%, respectively), and thus less affected by the detector deadtime. Obtaining a correct composition for Ti-rich carbides is challenging, due to the overlap of C_2^{+}, C_4^{2+}, and Ti^{2+} at m/n 24 Da, as well as the TiC^{2+}, TiN^{2+}, and TiO^{2+} overlaps [27]. These overlaps were considered when analysing the composition of the carbides. Furthermore, the carbide composition is normalized, leaving only the major elements, and excluding a halo of Ni, Co, and Al that mainly originates from the metal matrix.

3. Results

3.1. Overview

Cross-sections in directions parallel and perpendicular to the building direction show a high level of cracking (see Fig. 1). Higher magnification of the solidification crack surface shows dendritic arms and a high number of small particles (ca. 25–100 nm). The APT and TEM specimens were prepared from a fractured sample in areas with an evident solidification crack surface, distinguishable by their dendritic appearance, like the one shown in Fig. 1c).

3.2. TEM

A representative micrograph of the STEM/HAADF analysis can be seen in Fig. 2. The rough dendritic fracture surface covered with the Pt layer from specimen preparation is visible. A square where an EDX map was done is shown in a). In b) the corresponding elemental maps are shown. Different features are marked i-v in the cut out. On the surface of the solidification crack (that is not everywhere parallel with the beam), several spherical features, (i), are observed which are enriched in Cr, Mo, Ti, Nb and possibly Ta. These features are interpreted as being either carbides (Ti-rich) or borides (Cr- and Mo-rich), based on previous knowledge of expected phases and APT analyses shown below.

In addition to the spherical features, a number of protrusions (marked vi, vii, viii, and ix) are observed. The metallic contents from EDX spot analysis for these points are given in Table 3. Due to the protective layer deposited during FIB/SEM specimen preparation, C and Pt are detected in the surface protrusions, but are removed during normalisation. Although the metal matrix and the Pt capping are overlapping with the features, it is clear that the protrusions on the surface contain more Ti than the matrix. Additionally, Mo, Ta, and Nb are enriched in some of these particles present on solidification crack surfaces. Thus, they are interpreted as being carbides and borides on the crack surface. It is interesting to note that particle (vii) contains a significant amount of Mo, indicating varying compositions of these particles.

On the solidification crack surface between (vi) and (vii), the surface is parallel with the electron beam, and a thin, dark contrast line is seen in the HAADF micrograph. This is consistent with a thin (<10 nm) surface oxide layer.

Some features marked (ii), (iii), and (iv) were identified in the bulk material. The HAADF contrast suggests that (iv) contains heavier elements than ii) which is confirmed by the EDX maps showing higher Ti, Nb, Ta, and Mo contents for (iv). The volume (iii) appears darker in HAADF and contains more Al and O (not shown in map) which is interpreted as an aluminium oxide particle. Together, (ii), (iii), and (iv) suggest that the aluminium oxide in (iii) acted as nucleation point for a Ti-rich carbide with a rim enriched in heavier elements during solidification. A second volume (v) appears darker in HAADF contrast and is mainly enriched in Ti which suggests another Ti-rich carbide.

In Fig. 3, electron diffraction patterns of the matrix are shown for two zone axes. In these diffraction patterns, there are no superlattice reflections characteristic for the γ' phase visible, indicating these is no precipitation of γ' during solidification of IN738LC during LPBF.

3.3. APT

The average metal composition from APT, when only analysing volumes that did not contain any fracture surfaces or precipitates, is given in Table 4. The B and Zr contents in the matrix (0.03 at.% and 0.01 at.%, respectively) are lower than in the powder (0.16 at.% and 0.04 at.%, respectively).

Fig. 4 shows the Cr distribution in the as-printed bulk material to be uneven. Cr-depleted regions appear which are enriched in Ni, Al, and Ti, as seen in the proxigram in the same figure. The Cr radial distribution function (RDF) for the same analysis can be found in supplementary material Fig. S1. The composition in the middle of these features is around 66 at.% Ni, 11 at.% Al and 5 at.% Ti. There is also some Cr (8 at.%). The size of these features reaches up to roughly 5 nm in diameter. The lack of superlattice reflection in the TEM diffraction patterns together with the composition and size from APT suggest that these are γ' precursors rather than fully formed γ' precipitates.

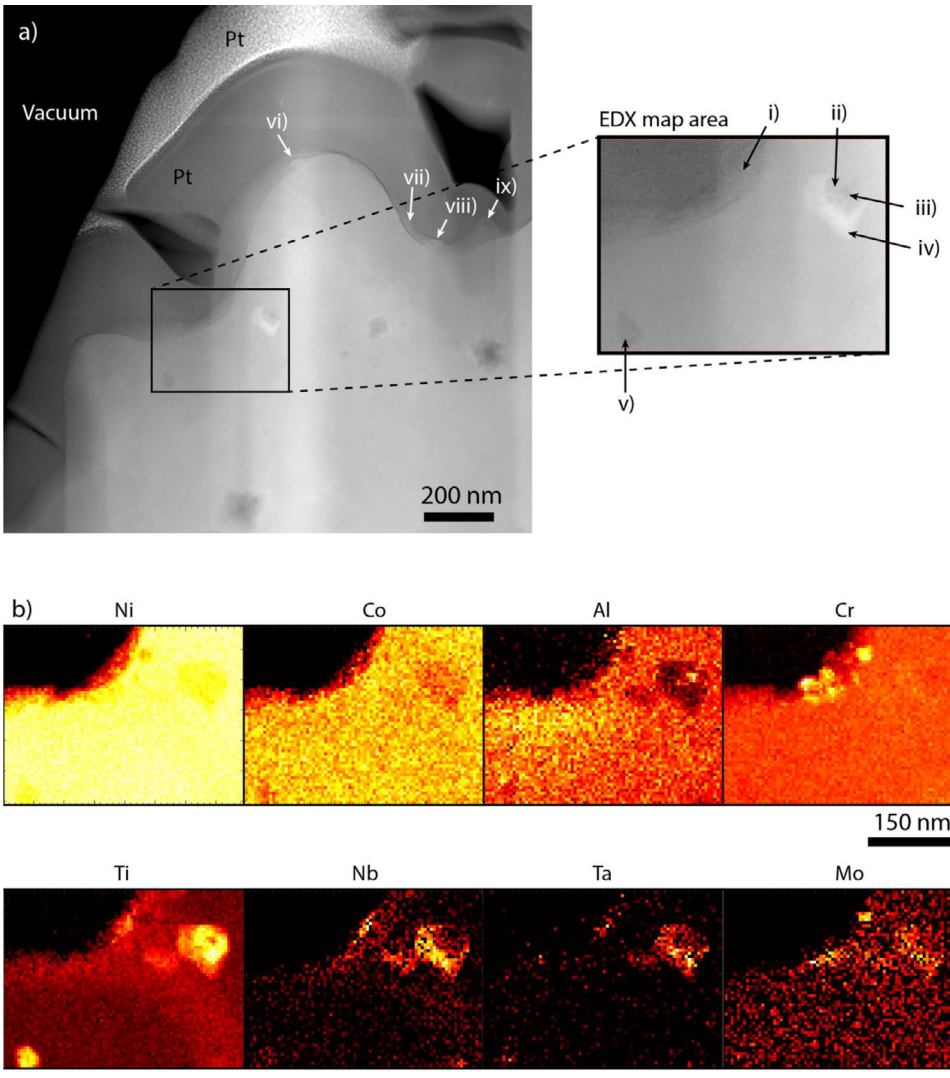

Fig. 2. (a) STEM/HAADF. The fracture surface is not straight along most of the edge. Some features are marked. (b) EDX map of the area marked in (a). Note that the colour-scale is different for the different elements, maximum values (white/light yellow) correspond to 71.9 at.% (Ni), 10.2 at.% (Co), 8.8 at.% (Al), 34.9 at.% (Cr), 16.8 at.% (Ti), 4.5 at.% (Nb), 1.7 at.% (Ta), and 3.4 at.% (Mo).

Table 3
Composition from spot EDX analysis in Fig. 2. C and Pt are not included. The location named "metal" is an average of 12 spot analyses in different locations of the matrix close to the fracture surface. Note that the structures are overlapping with the metal and the Pt coating in (vi) to (ix).

Location	*Ni (at.%)*	*Cr (at.%)*	*Co (at.%)*	*Al (at.%)*	*Ti (at.%)*	*Mo (at.%)*	*Nb (at.%)*	*Ta (at.%)*
metal	*64.0*	*16.8*	*8.5*	*5.3*	*3.1*	*0.8*	*0.7*	*0.8*
(vi)	*59.2*	*17.2*	*5.4*	*0.4*	*10.8*	*3.0*	*3.5*	*0.4*
(vii)	*35.6*	*16.9*	*8.7*	*0.0*	*15.1*	*16.9*	*6.8*	*0.0*
(viii)	*38.8*	*19.1*	*6.7*	*3.3*	*14.0*	*5.7*	*7.7*	*4.8*
(ix)	*4.4*	*10.3*	*0.0*	*0.0*	*62.0*	*7.3*	*4.8*	*11.3*

The volume, taken from another section of the same material directly by a fracture surface, was analysed using APT. On the fracture surface, carbides were found in three APT analyses, see two examples in Figs. 5 and 6. The occurrence of surface carbides in three out of five analyses of the fracture surface indicates a high number density of carbides, as neither the lift-out nor the tip sharpening specifically aim for the fracture surface carbides. The carbides are magnified in the reconstruction, due to their higher evaporation field, leaving the carbides as low density volumes (the so-called local magnification effect [21,28]). No elements were observed to segregate to the boundaries of the carbide found on the solidification crack surface.

Carbides were found in the metal matrix, away from the surface, seemingly aligned on a plane (Fig. 7). This specific analysis comes from a re-sharpened tip, and it is estimated that the tip of this reconstruction is located at around 300–800 nm distance from the fracture surface. No segregation was found on the plane between the carbides. Unlike the carbides in the solidification crack surface, the carbides in the bulk are surrounded by B atoms, as shown in Fig. 7band c. The different evaporation field of the carbide and the metal matrix during APT analysis causes trajectory aberrations, and thus result in a broadening of the layer of B atoms in the reconstruction.

The carbides (or carbo-oxo-nitrides as they also contain smaller amounts of O and N) contain mainly Ti and Cr as cations. They are also enriched in Mo, W, Ta, and Nb. The amount of the minor elements varies for different, even adjacent carbides. A careful deconvolution of the carbide content in combination with a C-13 correction for the C peak (see details in methods) gave the composition in Table 5 for the carbides observed in the analysis in Figs. 5–7 (as well as additional two samples

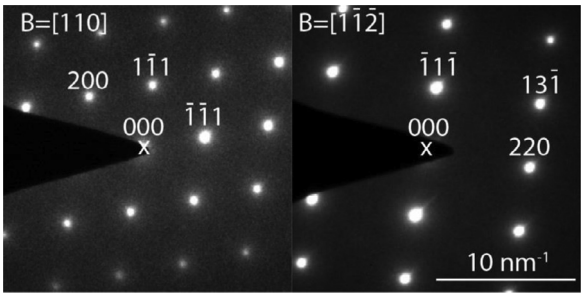

Fig. 3. Diffraction patterns of a grain of the bulk of the material.

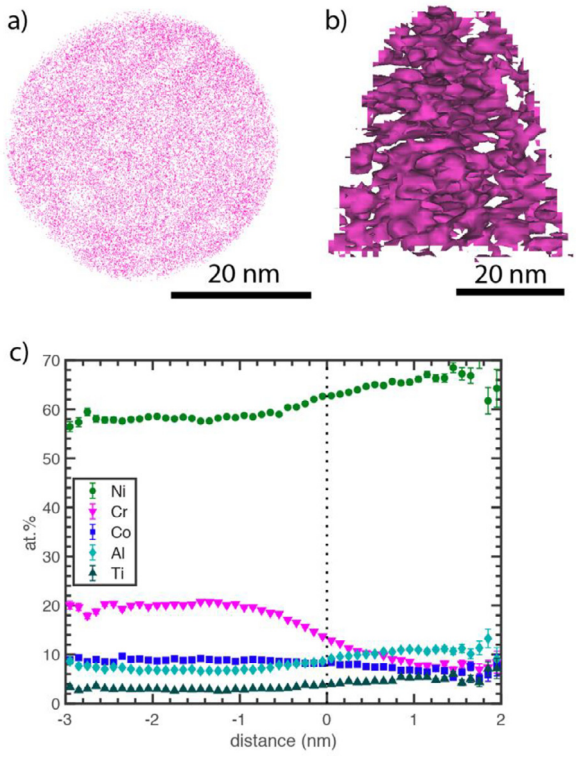

Fig. 4. (a) Cr distribution in a 5 nm thick slice of the metal. (b) Cr 15% isoconcentration surfaces. (c) a proxigram shows the Ni, Cr, Co, Al, and Ti content as a function of the distance to the isoconcentration surfaces in (b).

analysed). There was no significant difference between surface and bulk carbides. B is excluded as it can primarily be found on the metal/carbide interface. The stochiometric C+N+O content for MC-type carbides is 50 at.%, but MC carbides can be sub stochiometric [29]. After C-13 correction, the C+N+O content was found to be 45.9 at.%. It is also possible that these carbides are metastable (such as mentioned in [30]), as MC carbides seldom contain this high amount of Cr.

The average size of the carbides in Fig. 7 is estimated to be around 12 nm in diameter. The diameter is calculated from the number of atoms in the carbides, corrected for the detection efficiency of the instrument (37%), and assuming NaCl structure with a lattice parameter of 4.315 Å [31].

In one analysis, a boride was found directly by the oxide interface at the fracture surface, see Fig. 8. This boride cuts the edge of the APT analysis, and thus most of the boride is outside the analysed volume. Based on 3500 ions from the boride, the composition is roughly 25 at.% B, 43 at.% Cr, 14 at.% Ti, 10 at.% Mo, 4 at.% W, and minor amounts of Fe, Nb, and Ta. Some C is detected in the boride; however, this is assumed to (at least partly) originate from the Au layer which is contaminated with C and is therefore ignored in the normalised composition given.

Table 4
The composition of the Ni metal matrix, in APT reconstructions not containing any precipitates. The error given is the standard deviation between three APT analyses, one laser pulsed, and two voltage pulsed. All volumes come from the 1 µm closest to the solidification crack. All values are given in at.%.

Element	*Composition (at.%)*
Ni	*Bal.*
Cr	*17.5 ± 0.9*
Co	*8.8 ± 0.5*
Al	*8.1 ± 0.2*
Ti	*3.9 ± 0.5*
Mo	*1.0 ± 0.1*
W	*0.78±0.3*
Nb	*0.22±0.16*
C	*0.14±0.20*
Ta	*0.40±0.19*
Fe	*0.11±0.04*
Si	*0.07±0.01*
Zr	*0.01±0.01*
Mn	*0.01±0.01*
B	*0.03±0.01*
V	*0.01±0.02*

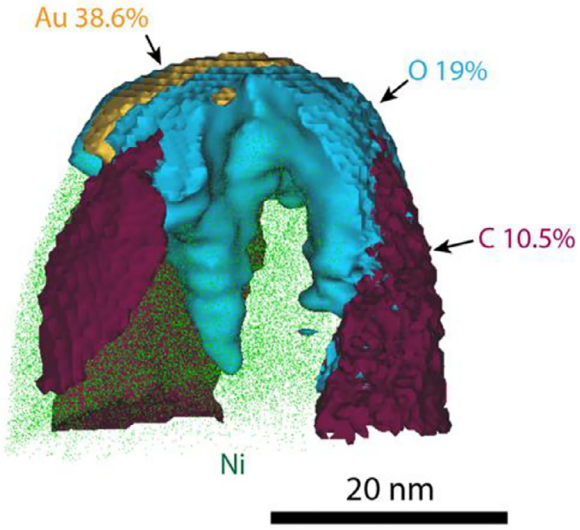

Fig. 5. Reconstruction of APT analysis. Isoconcentration surfaces corresponding to Au 38.6% (yellow), O 19% (blue) and C 10.5% (burgundy) are shown as well as a small part of the Ni atoms in the metal matrix. The values of the isoconcentration surfaces are set to visualize the different volumes in the best way. Three carbides, all cutting the edge of the analysis, are sitting in the oxide specimen surface.

Table 5
Composition of carbides, given in at.%. The error given is the standard deviation between the different analyses.

Element	*Composition (at.%)*
C	*37.7 ± 4.3*
N	*6.9 ± 1.9*
O	*1.3 ± 0.4*
Ti	*31.0 ± 2.6*
Cr	*11.3 ± 4.2*
Ta	*2.9 ± 1.1*
Mo	*4.3 ± 0.8*
Nb	*2.9 ± 0.6*
W	*1.8 ± 0.4*

Table 6
Oxide layer composition of the surface fracture after exposure to atmosphere. Average compositions and standard deviations from four analyses are given. The O content is probably somewhat underestimated.

Element	*O*	*Cr*	*Al*	*Ti*	*Zr*	*Nb*	*B*
Composition (at.%)	*50.9 ± 0.9*	*24.6 ± 3.8*	*10.1 ± 1.1*	*8.9 ± 1.5*	*3.8 ± 0.7*	*1.4 ± 0.7*	*≥0.2 ± 0.1*

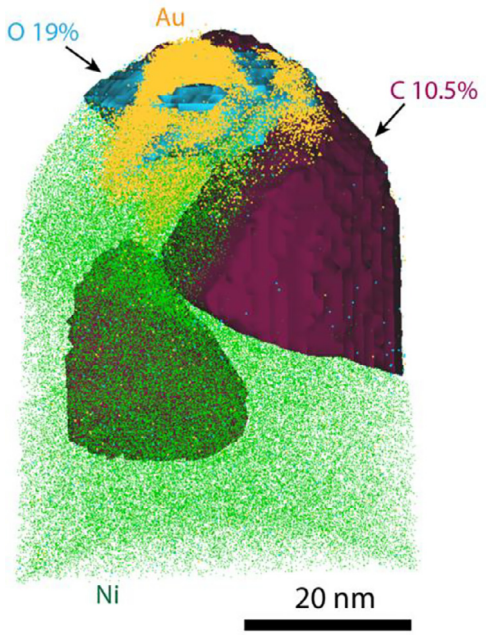

Fig. 6. Reconstruction of APT analysis. Isoconcentration surfaces corresponding O 19% (blue), and C 10.5% (burgundy) are shown as well as a small part of the Ni atoms (green) in the matrix and Au atoms (yellow) on the specimen surface. There are two carbides in this reconstruction, one sitting on the fracture surface.

The Cr-rich nature of this boride is consistent with the Cr-rich features in the STEM/EDX map in Fig. 7b.

Across five analyses, the Au-coating, surface oxide, and metal matrix were captured. The fracture surface has been exposed to air for approximately an hour before Au coating. The surface oxide was estimated to be less than 10 nm thick. The interface is rough at this scale, see for instance Fig. 5, where oxide can be seen penetrating into the metal. Although the mass spectra of mixed oxides are challenging to work with in APT due to the many molecular ions and overlaps [32], the oxide compositions were investigated. The average oxygen content of the analysed oxides was found to be 50.9 at.%, but it should be noted that it is common that the O content of oxides is somewhat underestimated in APT measurements [32–34]. Both Zr and B were present in the oxide. Zr was found to be evaporated mainly as ZrO^+, but also as ZrO^{2+}, $ZrO_2{}^+$, and $ZrO_3{}^{2+}$. B was found as B^{2+} (and B^+). The given B content in the oxide is a lower limit, as there are possibilities of complex ions containing B, but the mass spectra with the many peaks would overlap with these. For instance, BO^+ would be found mainly at m/n 27 Da, where Al^+, Cr^{2+} (and Fe^{2+}) also have peaks, making a deconvolution involving BO^+ virtually impossible. Furthermore, $BO_2{}^+$ would overlap with AlO^+ at 43 Da. Any Ni in the oxide was assumed to come from the bulk, as the very thin oxide in the APT reconstruction made the diffuse metal-oxide interface impossible to avoid. It is possible that the oxide contain a smaller amount (estimated to be less than 10 at.%) of Ni, but this not possible to determine from the data due to the oxide layer being very thin. For the same reason, Fe, Au, Co, Mo, Si, and P are assumed to originate from the bulk or coating and therefore removed from the total composition of the oxide.

The resulting oxide layer composition can be seen in Table 6. The composition is relatively similar in the different analyses of the oxide. However, the variation was larger than the counting error, and thus the standard deviation between the analyses is given in the table as the error. It is worth noting that both the B and Zr content are significantly higher than in the matrix of the metal (measured by APT to be 0.00–0.03 at.% and 0.02–0.04 at.%, respectively). This is in line with the reported oxide containing B and Zr at the cracked grain boundaries of LPBF processed IN738LC investigated by means of XPS, AES and APT [16].

3.4. Thermodynamic evaluation

The experimental findings were further investigated with respect to thermodynamic calculations using Thermo-Calc [35] and the TCNI11 database [36].

Thermo-Calc is commonly used for the calculation of thermodynamic and phase equilibria of multicomponent systems. In conjunction with suitable thermodynamic databases, assessed using the CALPHAD approach, Thermo-Calc can be used for a wide variety of applications, including Additive Manufacturing.

As solidification during Additive Manufacturing is non-equilibrium, the SCHEIL-module with solute trapping [37] and scanning speed of 1.15 m/s was used to examine the phase formation. For simplification, Fe as well as trace elements were excluded from the calculation. Based on the experimental investigation above, the η–phase Ni_3Ti was excluded from the simulation in favour of γ' formation. The predicted phases from the solidification simulation are (in order of formation): carbonitrides, FCC-matrix, γ' and borides. All of these phases were found in the experimental analysis. In the latest stage of solidification small amounts of Laves phase (Laves_C14) (less than 1%) was also predicted. This phase was not observed in the experimental work but due to the low amount predicted, its presence cannot reasonably be excluded. The simulation predicted the borides to be MB_2 (MB2_C32) while the composition from APT data is closer to M_2B-borides. It should be noted that both these borides have a positive driving force for formation meaning that both can form but the M_2B-boride would be meta-stable. In contrast to the boride formation from the liquid, where MB_2 is predicted to be the most stable, boride formation from the solid state where the matrix is formed predicts M_2B, MB and M_5B_3 as thermodynamically stable (see Fig. 9).

In Table 7, measured and calculated matrix compositions are displayed. The early stage of solidification was chosen for comparison since there is segregation in the matrix at this stage. As seen the agreement between the measured and calculated matrix composition is very good. The predicted composition of the γ' is 68 at.% Ni, 12 at.% Ti, 9% at.% Al and 3 at.% Cr, which is in line with the measured composition of the γ' precursors observed by APT (Fig. 4).

The composition of carbonitrides is changing drastically during solidification, making it difficult to compare the calculated results to the experimental data. At the beginning of solidification, Ti(C,N) with a high nitrogen content is predicted while in the middle of the solidification process Ti(C,N) is predicted to have a high carbon content. In contrast, during the last part of solidification, NbC is predicted. At all temperatures, other elements are predicted to dissolve within the carbonitrides, but it should be noted that the maximum Cr-content predicted is less than 1 at.%.

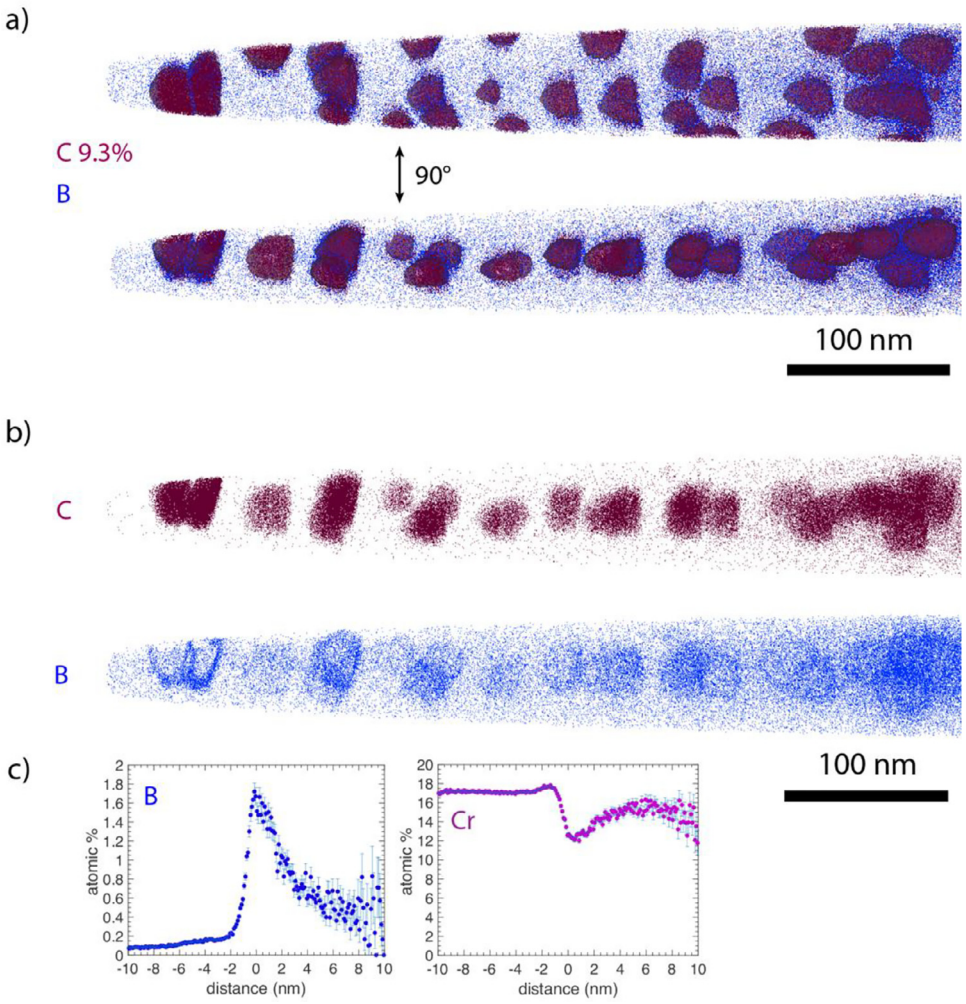

Fig. 7. APT analysis reconstruction of a volume containing carbides. (a) B atoms and C 9.3% isoconcentration surfaces show the outline of the layer of carbides. (b) C and B shown separately. In (c) the proxigram based on the C isoconcentration surfaces in (a) is shown to display B segregation to the carbide surfaces and the Cr concentration.

Table 7
The composition of the Ni metal matrix based on APT measurements and Thermo-Calc calculations.

Element	*Measured composition (at.%)*	*Calculated composition (at.%)*
Ni	*Bal.*	*Bal.*
Cr	*17.5 ± 0.9*	*18.2*
Co	*8.8 ± 0.5*	*8.9*
Al	*8.1 ± 0.2*	*6.9*
Ti	*3.9 ± 0.5*	*3.5*
Mo	*1.0 ± 0.1*	*1.1*
W	*0.78±0.3*	*0.86*
Nb	*0.22±0.16*	*0.42*
C	*0.14±0.20*	*0.17*
Ta	*0.40±0.19*	*0.56*
Zr	*0.01±0.01*	*0.02*
B	*0.03±0.01*	*0.08*

Based on the simulation Zr, B and Ti predominantly segregate to the liquid, with 1.4 at.% Zr, 4.0 at.% B and 18.4 at.% Ti in the last 1% of the liquid phase. This should be compared with the nominal composition of the powder with 0.04 at.% Zr, 0.16 at.% B and 3.93 at.% Ti respectively, see Table 1.

During the experimental investigation in this study, some oxide formation was observed supporting previous XPS and AES analyses for this material [16] which indicated the formation of complex oxides [16]. A detailed analysis of the possible liquid to atmosphere reaction was therefore performed using TCOX11 database [38]. The calculations show that at relatively low partial pressure of O_2, corundum (M_2O_3) forms preferentially. The corundum is predicted to contain 28 at.% Cr, 11 at.% Al and some Ti (less than 1 at.%). This is in good agreement with oxide composition measured during APT analysis considering Cr and Al, see Table 6. The reason for the deviation between measured and predicted oxide Ti content could be that the calculation was done for the nominal composition, but as seen above there is a strong segregation of Zr and Ti to liquid phase during solidification. It is relevant to note that Zr is not included in the description of Corundum in TCOX11, so the Zr solubility could not be predicted.

4. Discussion

Historically, B and Zr were added to nickel-based superalloys to improve fluidity during casting and to enhance creep and tensile properties. However, both elements have been linked to cracking sensitivity of nickel-based superalloys that are manufactured using LPBF and EBM [2,4,5,9–11,14].

The initial study of the IN738LC variant with increased B and Zr contents by Gruber et al. [16] showed that these elements have a detrimental effect when manufacturing the material by LPBF leading to cracks along HAGBs with decohesion facets. The current study was conducted to investigate this material variant and especially the fracture surfaces in more detail.

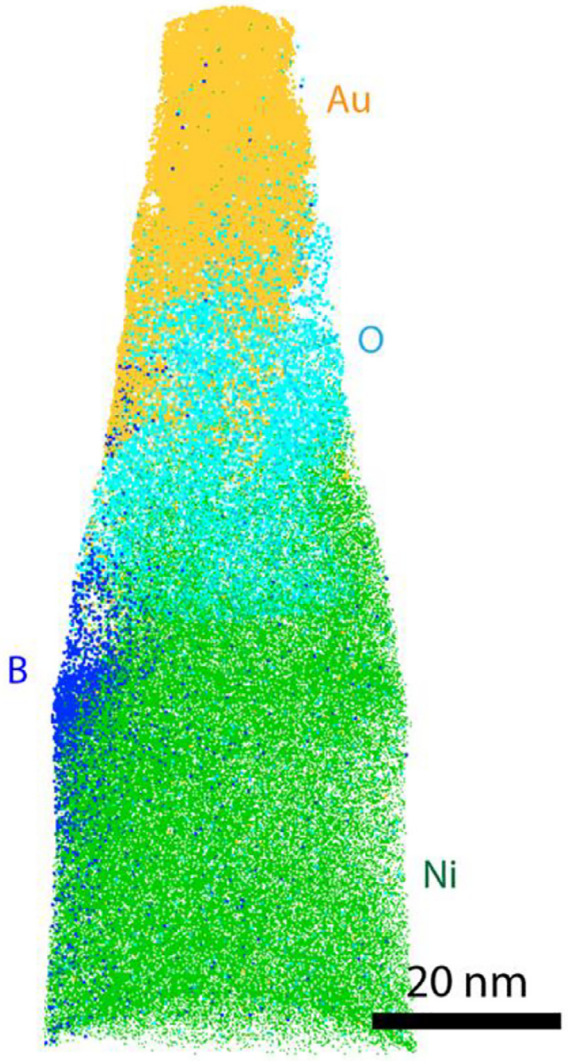

Fig. 8. APT reconstruction of material HB-HZr. Au, O, B, and Ni atoms are shown. A boride is located at the fracture surface.

4.1. Bulk material

Analysis of the bulk material using APT in Fig. 4 showed small features denuded of Cr and enriched in Ti and Al. However, TEM diffraction analysis in Fig. 3 indicated the absence of fully formed γ' precipitates which leads to hypothesis that these features are γ' precursors. These results agree with findings by Jägle et al. who reported that no coherent γ' phase was found in as-printed LPBF IN738LC material despite thermodynamic predictions of its formation [18]. As the γ' phase is highly important for nickel-based superalloys, the formation of these particles in additively manufactured material is of interest and will be subject of a future study.

APT analysis of the bulk material (Fig. 7) showed a vast number of small carbides (~12 nm in diameter) which seem to be evenly distributed alongside a 2D plane in the bulk. These carbides are MC carbides with Ti and Cr as the most abundant metallic elements and have previously been reported in the as-built microstructure of LPBF superalloys [15,18]. The Cr concentration profile suggests that Cr is being pushed out from these carbide particles which would agree with the equilibrium content being less than 1 at.%, resulting in a driving force for Cr to diffuse out from these carbides. The MC (or metastable) carbides found in the bulk by APT are smaller than some of the carbides observed by TEM (up to 100 nm), indicating a significant spread in sizes of these carbides. On the metal/carbide interface, B atoms are found to segregate.

The average metal composition as measured from APT volumes that did not contain any fracture surfaces or carbides showed that the B and Zr concentration was overall about 5 times lower in the bulk material compared to the powder material (see Table 4). Zr was not found in any of the features observed in the bulk material, suggesting that it segregates more strongly to the grain boundaries, as supported by Thermo-Calc simulations indicating segregation to the last solidified liquid. This is also supported by previous findings which reported that particularly B and Zr partition to a liquid film phase along grain boundaries in IN738LC [4,5].

4.2. Crack surface

The previous study established that the observed cracks in the HB-HZr IN738LC material were located along HAGBs and investigated the fracture surfaces using XPS and AES [16]. Other authors [4,5] investigated grain boundary chemistry of AM IN738LC in detail and identified low-melting phases high in B and Zr as likely reasons for cracking. The current TEM and APT findings, and Thermo-Calc simulations combined with previous XPS and AES results support this hypothesis. XPS analysis showed that B and Zr are significantly enriched on the fracture surface, reaching B levels of up to 2.8 at.%) and Zr levels up to 1 at.% [16]. This increased amount of both elements on the fracture surface agrees with the APT analysis of the surface oxide, and the bulk material showing lower concentration levels of both B and Zr. The fracture surface was exposed to air during specimen preparation as the material could not be opened in the FIB/SEM, as compared to specimen fracture in ultra-high vacuum during XPS analysis, reported by Gruber et al. [16]. Therefore, it is not possible to conclude from APT analysis alone whether the Zr-oxide is formed during solidification or during exposure of the fracture surface. However, the presence of Zr in the APT analysis in this work agrees with previous XPS and AES analyses [16] and was further confirmed by thermodynamic calculations of the oxide stability in the system. The difference in B content between the XPS (up to 2.8 at.%) and APT (≥0.2 at.%) measurements can be due to several factors. First of all, the APT is position sensitive, and a boride was found on the crack surface. In APT precipitates can be analysed separately, but in XPS the borides contribute to the total composition of the surface oxide. In APT, the overlap issues in the mass spectrum give a possible underestimation, as described above. Lastly, it is also possible that B could have sublimated during the exposure to air or Au deposition prior to APT specimen preparation, as the sample could not be opened in vacuum.

A Cr-rich boride on the solidification crack surface was detected by APT (see Fig. 8) which also contains Mo and Ti. This is in line with some of the features observed in TEM (see Fig. 2). It is possible that these particles have a similar nature. If not considering the Ti content, the composition of the observed boride (M_2B) is in line with what others have identified in nickel-based superalloys manufactured by AM [4,15]. The presence of Ti could be an indication that it is a nonequilibrium precursor, or a different phase, but it could also be an indication of a boride sitting next to a carbide. Thermodynamic calculations show a high stability of borides in the studied system, with MB_2 or metastable M_2B as possible candidates, described above.

The previous study identified several carbides on the fracture surfaces which were also found during TEM (see Fig. 2 pos. ix) as well as APT analyses and were identified as Ti-rich MC carbides. In the current study, APT analyses showed that B is evenly distributed in the oxide layer. While bulk carbides were found to be surrounded with a B layer, analysis of the volume directly by fracture surface carbides shows no increased B levels surrounding these carbides (see Figs. 5 and 6). It is possible that any B is dissolved in the oxide rather than segregating to the carbide interface in these cases.

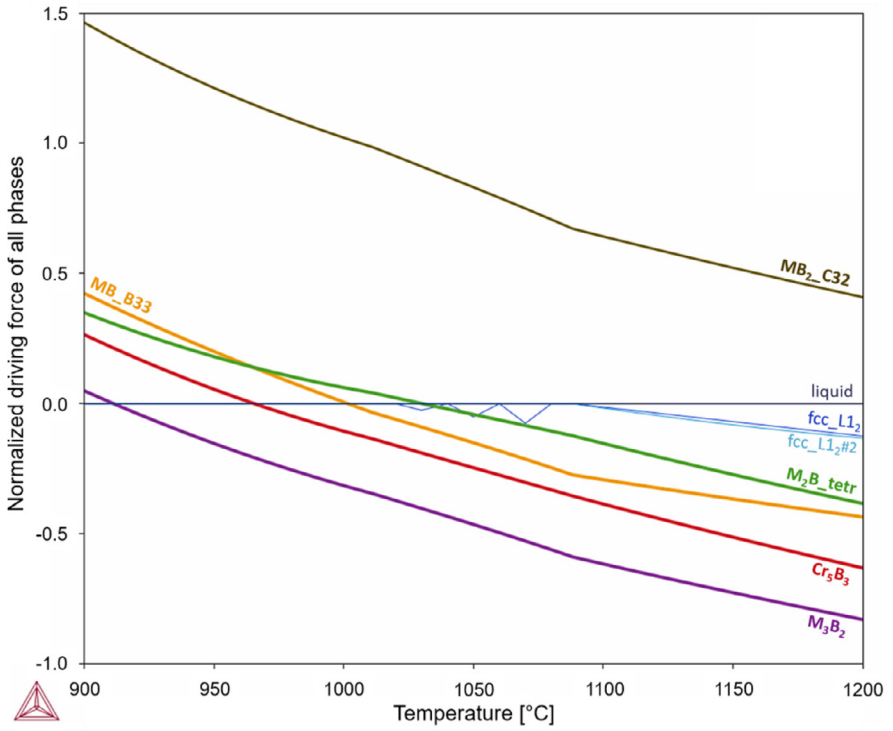

Fig. 9. Thermodynamic prediction of boride formation in IN738LC with formation from the liquid for positive driving forces (with MB_2 as most stable boride) and formation from the solid state for negative driving forces (with M_2B, MB, and M_5B_3 as stable borides).

5. Conclusions

This study used APT and TEM analysis to investigate a variant of the nickel-based superalloy IN738LC, manufactured by LPBF, containing high levels of B (0.03 wt.%) and Zr (0.07 wt.%) to reveal the impact of these micro-alloying elements on the crack formation during LPBF processing. The TEM and APT findings supported by Thermo-Calc simulations presented in this study combined with previous XPS and AES results support the hypothesis that low-melting phases high in B and Zr are likely reasons for cracking of AM IN738LC. The following conclusions can be drawn:

- APT analysis detected Zr and small amounts of B in the oxide layers on the fracture surfaces of samples opened in air. Thermodynamic calculations suggest that both Zr and B segregate strongly to the last fraction of the liquid phase during solidification. The high oxygen potential and high oxygen affinity of Zr and B would result in their further oxidation. This supports the hypothesis that the cracking in the high Zr and B material occurs due to a liquid oxide film formed at high angle grain boundaries.
- On the crack surfaces, Ti- and Cr-rich M(C,N), as well as Cr, Mo, and Ti-rich borides are found. The presence of Ti in the borides could indicate their nonequilibrium state and thermodynamic calculations suggest MB_2 and M_2B as likely compositions. It is possible that due to the complex thermal history of the material metastable borides form in nickel-based superalloys manufactured by AM.
- In the bulk metal, Cr-denuded zones of a few nanometres are observed which are enriched in Al and Ti. However, the absence of superlattice reflection points in the TEM diffraction patterns and the small size (~5 nm in diameter) suggest that these areas are γ' precursors rather than fully formed γ' particles.
- A high number of Ti- and Cr-rich M(C,N) are in the bulk material. The Cr concentration profile suggests that Cr is pushed out of these carbides, indicating a non-equilibrium composition, B was found in thin layers surrounding the carbides located in the bulk at the metal/carbide interfaces.

Declaration of Competing Interest

The authors declare that they have no known competing financial interests or personal relationships that could have appeared to influence the work reported in this paper.

CRediT authorship contribution statement

Kristina Lindgren: Conceptualization, Investigation, Methodology, Formal analysis, Writing – original draft, Writing – review & editing, Visualization. **Fiona Schulz:** Conceptualization, Writing – original draft, Writing – review & editing. **Hans Gruber:** Conceptualization, Investigation, Writing – review & editing. **Andreas Markström:** Software, Writing – original draft, Writing – review & editing. **Eduard Hryha:** Conceptualization, Writing – review & editing, Project administration, Funding acquisition.

Acknowledgements

This work has been performed in the framework of the project "Tailored Materials for Additive Manufacturing (MADAM)" and the Centre for Additive Manufacturing – Metal (CAM^2), all supported by the Swedish Governmental Agency of Innovation Systems (Vinnova). Support from the Area of Advance Production at Chalmers are also acknowledged. The APT and TEM was performed in the Chalmers Materials Analysis Laboratory (CMAL). Olof Bäcke is acknowledged for support with the TEM and Mattias Thuvander and Krystyna Stiller for fruitful discussions.

Supplementary materials

Supplementary material associated with this article can be found, in the online version, at doi:10.1016/j.mtla.2022.101609.

References

[1] M.M. Attallah, R. Jennings, X. Wang, L.N. Carter, Additive manufacturing of Ni-based superalloys: the outstanding issues, MRS Bull. 41 (10) (2016) 758–764.

[2] E. Chauvet, P. Kontis, E.A. Jägle, B. Gault, D. Raabe, C. Tassin, J.J. Blandin, R. Dendievel, B. Vayre, S. Abed, G. Martin, Hot cracking mechanism affecting a non-weldable Ni-based superalloy produced by selective electron Beam Melting, Acta Mater. 142 (2018) 82–94.

[3] R. Engeli, T. Etter, S. Hövel, K. Wegener, Processability of different IN738LC powder batches by selective laser melting, J. Mater. Process. Technol. 229 (2016) 484–491.

[4] P. Kontis, E. Chauvet, Z. Peng, J. He, A.K. da Silva, D. Raabe, C. Tassin, J.J. Blandin, S. Abed, R. Dendievel, B. Gault, G. Martin, Atomic-scale grain boundary engineering to overcome hot-cracking in additively-manufactured superalloys, Acta Mater. 177 (2019) 209–221.

[5] M. Cloots, P.J. Uggowitzer, K. Wegener, Investigations on the microstructure and crack formation of IN738LC samples processed by selective laser melting using Gaussian and doughnut profiles, Mater. Des. 89 (2016) 770–784.

[6] L.N. Carter, M.M. Attallah, R.C. Reed, Laser powder bed fabrication of nickel-base superalloys: influence of parameters; characterisation, quantification and mitigation of cracking, superalloys 2012, TMS, 2012.

[7] O. Adegoke, J. Andersson, H. Brodin, R. Pederson, Review of laser powder bed fusion of gamma-prime-strengthened nickel-based superalloys, Metals 10 (8) (2020) 996, doi:10.3390/met10080996.

[8] M.J. Donachie, S. Donachie, Superalloys: A Technical Guisw, ASM International, 2002.

[9] W. Zhou, G. Zhu, R. Wang, C. Yang, Y. Tian, L. Zhang, A. Dong, D. Wang, D. Shu, B. Sun, Inhibition of cracking by grain boundary modification in a non-weldable nickel-based superalloy processed by laser powder bed fusion, Mater. Sci. Eng. A 791 (2020) 139745, doi:10.1016/j.msea.2020.139745.

[10] N. Wang, S. Mokadem, M. Rappaz, W. Kurz, Solidification cracking of superalloy single- and bi-crystals, Acta Mater. 52 (11) (2004) 3173–3182.

[11] B.I. Kang, C.H. Han, Y.K. Shin, J.I.L. Youn, Y.J. Kim, Effects of boron and zirconium on grain boundary morphology and creep resistance in nickel-based superalloy, J. Mater. Eng. Perform. 28 (11) (2019) 7025–7035.

[12] M. Vilanova, M.C. Taboada, A. Martinez-Amesti, A. Niklas, M. San Sebastian, T. Guraya, Influence of minor alloying element additions on the crack susceptibility of a nickel based superalloy manufactured by LPBF, Materials 14 (19) (2021) 5702 (Basel), doi:10.3390/ma14195702.

[13] D. Heydari, A.S. Fard, A. Bakhshi, J.M. Drezet, Hot tearing in polycrystalline Ni-based IN738LC superalloy: influence of Zr content, J. Mater. Process. Technol. 214 (3) (2014) 681–687.

[14] A. Després, S. Antonov, C. Mayer, C. Tassin, M. Veron, J.J. Blandin, P. Kontis, G. Martin, On the role of boron, carbon and zirconium on hot cracking and creep resistance of an additively manufactured polycrystalline superalloy, Materialia 19 (2021) 101193, doi:10.1016/j.mtla.2021.101193.

[15] A. Després, C. Mayer, M. Veron, E.F. Rauch, M. Bugnet, J.J. Blandin, G. Renou, C. Tassin, P. Donnadieu, G. Martin, On the variety and formation sequence of second-phase particles in nickel-based superalloys fabricated by laser powder bed fusion, Materialia 15 (2021) 101037, doi:10.1016/j.mtla.2021.101037.

[16] H. Gruber, E. Hryha, K. Lindgren, Y. Cao, M. Rashidi, L. Nyborg, The effect of boron and zirconium on the microcracking susceptibility of IN-738LC derivatives in laser powder bed fusion, Appl. Surf. Sci. 573 (2022) 151541, doi:10.1016/j.apsusc.2021.151541.

[17] E. Hryha, E. Rutqvist, J. Björkvall, L. Nyborg, Development of methodology for surface characterization of vanadium containing slag, Surf. Interface Anal. 46 (10–11) (2014) 984–988.

[18] E.A. Jägle, Z. Sheng, L. Wu, L. Lu, J. Risse, A. Weisheit, D. Raabe, Precipitation reactions in age-hardenable alloys during laser additive manufacturing, JOM 68 (3) (2016) 943–949.

[19] D.J. Larson, D.T. Foord, A.K. Petford-Long, H. Liew, M.G. Blamire, A. Cerezo, G.D.W. Smith, Field-ion specimen preparation using focused ion-beam milling, Ultramicroscopy 79 (1–4) (1999) 287–293.

[20] K. Thompson, D. Lawrence, D.J. Larson, J.D. Olson, T.F. Kelly, B. Gorman, *In situ* site-specific specimen preparation for atom probe tomography, Ultramicroscopy 107 (2–3) (2007) 131–139.

[21] M.K. Miller, R.G. Forbes, Atom-Probe Tomography: The Local Electrode Atom Probe, Springer, New York, 2014.

[22] D.R. Kingham, The post-ionization of field evaporated ions: a theoretical explanation of multiple charge states, Surf. Sci. 116 (1982) 273–301.

[23] T.T. Tsong, Field ion image formation, Surf. Sci. 70 (1978) 211–233.

[24] M.K. Miller, Atom Probe Tomography: Analysis at the Atomic Level, Kluwer Academic/Plenum Publishers, New York, 2000.

[25] O.C. Hellman, J.A. Vandenbroucke, J. Rüsing, D. Isheim, D.N. Seidman, Analysis of three-dimensional atom-probe data by the proximity histogram, Microsc. Microanal. 6 (5) (2000) 437–444.

[26] M. Thuvander, J. Weidow, J. Angseryd, L.K. Falk, F. Liu, M. Sonestedt, K. Stiller, H.O. Andren, Quantitative atom probe analysis of carbides, Ultramicroscopy 111 (6) (2011) 604–608.

[27] J. Angseryd, F. Liu, H.O. Andren, S.S. Gerstl, M. Thuvander, Quantitative APT analysis of Ti(C,N), Ultramicroscopy 111 (6) (2011) 609–614.

[28] E.A. Marquis, J.M. Hyde, Applications of atom-probe tomography to the characterisation of solute behaviours, Mater. Sci. Eng. R Rep. 69 (4–5) (2010) 37–62.

[29] C-Ti Binary Phase Diagram 0-100 at.% Ti: Datasheet from "PAULING FILE Multinaries Edition", SpringerMaterials, 2012 https://materials.springer.com/isp/phase-diagram/docs/c_0100118 in: P. Villars, H. Okamoto (Eds.) Springer-Verlag Berlin Heidelberg & Material Phases Data System (MPDS), Switzerland & National Institute for Materials Science (NIMS), Japan 2022.

[30] J. Xu, P. Kontis, R.L. Peng, J. Moverare, Modelling of additive manufacturability of nickel-based superalloys for laser powder bed fusion, Acta Mater. 240 (2022).

[31] TiC Crystal StructureDatasheet from "PAULING FILE Multinaries Edition", SpringerMaterials, 2012 https://materials.springer.com/isp/crystallographic/docs/sd_0261188 in: P. Villars, K. Cenzual (Eds.) Springer-Verlag Berlin Heidelberg & Material Phases Data System (MPDS), Switzerland & National Institute for Materials Science (NIMS), Japan.

[32] K. Lindgren, P. Domstedt, P. Szakalos, M. Thuvander, The Nanostructure of the Oxide Formed on Fe-10Cr-4Al Exposed in Liquid Pb, Microsc. Microanal. (2021) 1–14.

[33] J. Maier, B. Pfeiffer, C.A. Volkert, C. Nowak, Three-dimensional microstructural characterization of lithium manganese oxide with atom probe tomography, Energy Technol. 4 (12) (2016) 1565–1574.

[34] A. Devaraj, R. Colby, W.P. Hess, D.E. Perea, S. Thevuthasan, Role of photoexcitation and field ionization in the measurement of accurate oxide stoichiometry by laser-assisted atom probe tomography, J. Phys. Chem. Lett. 4 (6) (2013) 993–998.

[35] J.O. Andersson, T. Helander, L. Höglund, P. Shi, B. Sundman, THERMO-Calc & DICTRA, computational tools for materials science, Calphad 26 (2002) 273–312.

[36] Thermo-Calc software Ni-based superalloys database, version 11, (2022 a release).

[37] Thermo-Calc Documentation Set, (version 2022a (accessed 8 December 2021)).

[38] Thermo-Calc Software Metal Oxide Solutions database, version 11, (2022 a release).